MusE GAs FLOw and Wind (MEGAFLOW) IV. A two sightline tomography of a galactic wind

Johannes Zabl,[1⋆] Nicolas F. Bouché,[1] Ilane Schroetter,[2] Martin Wendt,[3] Thierry Contini,[4] Joop Schaye,[5] Raffaella A. Marino,[6] Sowgat Muzahid,[5] Gabriele Pezzulli,[6] Anne Verhamme,[7] Lutz Wisotzki[8]

[1] *Univ Lyon, Univ Lyon1, Ens de Lyon, CNRS, Centre de Recherche Astrophysique de Lyon UMR5574, F-69230 Saint-Genis-Laval, France*
[2] *GEPI, Observatoire de Paris, CNRS-UMR8111, PSL Research University, Univ. Paris Diderot, 5 place Jules Janssen, 92195 Meudon, France*
[3] *Institut für Physik und Astronomie, Universität Potsdam, Karl-Liebknecht-Str. 24/25, 14476 Golm, Germany*
[4] *Institut de Recherche en Astrophysique et Planétologie (IRAP), Université de Toulouse, CNRS, UPS, F-31400 Toulouse, France*
[5] *Leiden Observatory, Leiden University, PO Box 9513, NL-2300 RA Leiden, the Netherlands*
[6] *Department of Physics, ETH Zürich,Wolfgang-Pauli-Strasse 27, 8093 Zürich, Switzerland*
[7] *Observatoire de Genéve, UniversitÃl' de Genéve, 51 Ch. des Maillettes, 1290 Versoix, Switzerland*
[8] *Leibniz-Institut für Astrophysik Potsdam (AIP), An der Sternwarte 16, 14482 Potsdam, Germany*

Accepted XXX. Received YYY; in original form ZZZ

ABSTRACT

Galactic outflows are thought to eject baryons back out to the circum-galactic medium (CGM). Studies based on metal absorption lines (Mg II in particular) in the spectra of background quasars indicate that the gas is ejected anisotropically, with galactic winds likely leaving the host in a bi-conical flow perpendicular to the galaxy disk. In this paper, we present a detailed analysis of an outflow from a $z = 0.7$ "green-valley" galaxy ($\log(M_*/M_\odot) = 9.8$; SFR $= 0.5\,M_\odot\,yr^{-1}$) probed by two background sources from the MUSE Gas Flow and Wind (MEGAFLOW) survey. Thanks to a fortuitous configuration with a background quasar (SDSSJ1358+1145) and a bright background galaxy at $z = 1.4$, both at impact parameters of ≈ 15 kpc, we can – for the first time – probe *both* the receding and approaching components of a putative galactic outflow around a distant galaxy. We measure a significant velocity shift between the Mg II absorption from the two sightlines ($84 \pm 17\,km\,s^{-1}$), which is consistent with the expectation from our simple fiducial wind model, possibly combined with an extended disk contribution.

Key words: galaxies: evolution – galaxies: haloes – intergalactic medium – quasars: absorption lines – quasars: individual: SDSSJ1358+1145

1 INTRODUCTION

Galaxies are surrounded by a complex multi-phase medium, the circumgalactic medium (CGM; Tumlinson et al. 2017 for a recent review). Accretion from this CGM onto galaxies and winds from the galaxies into the CGM are believed to be key ingredients in regulating the evolution of galaxies.

The detailed study of absorption features detected in bright background sources is one of the main observational tools helpful in characterizing the physical properties and kinematics of the CGM gas. Among various transitions, the Mg II$\lambda\lambda$2797, 2803 doublet is an especially useful tracer of the cool, photo-ionized component of the CGM ($T \approx 10^{4-5}$K; e.g., Bergeron & Stasińska 1986). Its strength, easy identifiability as a doublet, and convenient rest-frame wavelength have allowed the collection of large statistical samples of Mg II absorbers (e.g. Lanzetta et al. 1987; Steidel & Sargent 1992; Nestor et al. 2005; Zhu & Ménard 2013) at redshifts $0.1 \lesssim z \lesssim 2.5$. Follow-up observations of the fields surrounding the absorbers have identified galaxies associated to the absorbers and, hence, clearly established that the Mg II absorbing gas is found in the haloes of galaxies (e.g. Bergeron 1988; Bergeron & Boissé 1991; Steidel 1995; Steidel et al. 2002; Nielsen et al. 2013a,b).

Subsequently, large observational efforts have been put into mapping the spatial distribution and kinematics of the Mg II absorbing gas w.r.t. the galaxies in whose haloes the gas resides. The major result from these studies is that the Mg II absorbing gas is not isotropically distributed around the galaxies (e.g. Bordoloi et al. 2011; Bouché et al. 2012; Kacprzak et al. 2012; Lan et al. 2014; Lan & Mo 2018; Zabl et al. 2019; Martin et al. 2019;

⋆ E-mail: johannes.zabl@univ-lyon1.fr

Schroetter et al. 2019). Instead, the observations support a two-component geometry: a bi-conical outflow perpendicular to the galaxy disk and an extended gas disk approximately co-planar with the stellar disk. This allows to split the Mg II absorber sightlines into an outflow and a disk sub-sample, which can be used to study the kinematics of the outflows (e.g. Bouché et al. 2012; Kacprzak et al. 2014; Muzahid et al. 2015; Schroetter et al. 2015, 2016, 2019; Rahmani et al. 2018b; Martin et al. 2019) and the extended gas accretion disks (e.g. Steidel et al. 2002; Chen et al. 2005; Kacprzak et al. 2010, 2011b; Bouché et al. 2013, 2016; Ho et al. 2017; Ho & Martin 2019; Rahmani et al. 2018a; Zabl et al. 2019), respectively.

The aforementioned results have been obtained statistically by collecting single sightlines around *many galaxies*. A step forward would be to directly map the geometry of the CGM around *individual galaxies*. Such "tomography" requires multiple or very extended bright background sources behind the CGM of an individual galaxy.

Taking advantage of the comparably large extent that galaxies in the local Universe span on the sky, Bowen et al. (2016) have used four different background quasars to firmly conclude for an individual galaxy that the absorbing gas is distributed in an extended gas disk. However, having multiple sufficiently bright background galaxies covering the halo of a single galaxy is rare, especially at high redshift where the virial radius corresponds to a fraction of an arcminute.

The few studies beyond the local Universe were either using quasars by chance aligned close to each other (e.g. D'Odorico et al. 1998; Crighton et al. 2010; Muzahid 2014), multiple imaged lensed-quasar pairs (e.g. Rauch et al. 1999; Lopez et al. 1999, 2007; Ellison et al. 2004; Rubin et al. 2018), or extended galaxies (e.g. Péroux et al. 2018; Lopez et al. 2018, 2019). The main focus of these studies was to characterize the coherence scale of the absorbing gas.

In this paper, we present a tomographic study of the CGM around a $z = 0.70$ galaxy surrounded by two bright background sightlines which was discovered in the MUSE Gas FLow and Wind (MEGAFLOW) survey (Schroetter et al. 2016 -paper I-; Zabl et al. 2019 -paper II-; Schroetter et al. 2019 -paper III-). This survey consists of 79 strong Mg II absorbers towards 22 quasar sightlines which have been selected to have (at least) three Mg II absorbers with rest-frame equivalent widths $\mathrm{EW}_0^{\lambda 2796} > 0.3$ Å and $0.4 < z_{\mathrm{abs}} < 1.5$.

The paper is organized as follows. We present our observations in §2, the galaxies and absorption sightlines in the field in §3, and a model for the CGM in §4. We compare this CGM model to our data and discuss our results in §5. Finally, we present our conclusions in §6. Throughout, we use a 737 cosmology ($H_0 = 70$ km s^{-1}, $\Omega_{\mathrm{m}} = 0.3$, and $\Omega_\Lambda = 0.7$) and we state all distances as 'proper' (physical) distances. A Chabrier (2003) stellar Initial Mass Function (IMF) is assumed. We refer to the [O II] $\lambda\lambda$3727, 3729 doublet simply as [O II]. All wavelengths and redshifts are in vacuum and are corrected to a heliocentric velocity standard.

2 OBSERVATIONS

2.1 MUSE data

We observed the field around the quasar SDSSJ1358+1145 with MUSE (Multi Unit Spectroscopic Explorer; Bacon et al. 2006, 2010) for a total integration time of 3.11 hr. The first four exposures (4x1500 s=1.67 hr; 2016-04-09), which constitute the data used in papers II&III, were taken with the nominal wide field mode without adaptive optics (AO) (WFM-NOAO-N), as MUSE's AO system was not yet available at the time. After identifying the science case of the present work, we realized a potential benefit from using MUSE's extended mode for subsequent observations of the field. Therefore, we completed the observations in extended wide field mode, while additonally taking advantange of the available AO (4x1300 s=1.44 hr; 2018-03-14; WFM-AO-E). Extended mode increases the blue wavelength coverage from 4750 Å to 4600 Å with the trade-off of some second order contamination at wavelengths $\gtrsim$ 8000 Å. The extra coverage helps to better constrain the continuum around Mg II λ2796 at $z = 0.704$, the redshift of the foreground galaxy whose CGM we study in this work.

We reduced the data identically to paper II, except that we were using DRSv2.4 (Weilbacher et al. 2012, 2014, 2016), which allows for the reduction of the AO data. The combined AO and non-AO data have a point source Moffat full width at half maximum (FWHM) of 0″.55 at 7050 Å. Using the depth estimator from paper II, this exposure time (3.11 hr) and this seeing results in an [O II] point source detection limit of 2.7×10^{-18} erg s^{-1} cm^{-2}. [1]

2.2 UVES data

We observed the quasar SDSSJ1358+1145 with the VLT high-resolution spectrograph UVES (Ultraviolet and Visual Echelle Spectrograph; Dekker et al. 2000) for a total integration time of 2966 s in the night of 2016-04-07. Further details about observation, reduction, and continuum normalisation are given in paper II.

3 RESULT

3.1 Identification of background sightlines

The main galaxy at $z = 0.704$ (*main*) was discovered through association with an $\mathrm{EW}_0^{\lambda 2796} = 2.5$ Å Mg II absorber towards the quasar SDSSJ1358+1145 from MEGAFLOW at an impact parameter of $b = 2''.3$ (16.8 kpc).

This quasar sightline is particularly interesting as it contains two additional very strong Mg II absorbers with a rest-frame equivalent width $\mathrm{EW}_0^{\lambda 2796} = 1.8$ and 2.6 Å at redshifts $z_{\mathrm{abs}} = 0.81$ and 1.42, respectively. The galaxy counterparts of the $z_{\mathrm{abs}} = 0.81$ and $z_{\mathrm{abs}} = 1.42$ absorbers have been described in paper III (wind sample) and paper II (accretion sample), respectively. They are galaxies with $\log(M_*/\mathrm{M}_\odot)$ of 9.3 and 9.9, and are at relatively small impact parameters of 1″.6 and 3″.6 from the quasar, as also expected from the known Mg II EW–impact parameter

[1] The estimate is for ≈ 7000 Å. The detection limits are higher at shorter and longer wavelengths (see e.g. Bacon et al. 2017).

anti-correlation (e.g. Lanzetta & Bowen 1990; Bouché et al. 2006; Kacprzak et al. 2011a; Chen et al. 2010; Nielsen et al. 2013b). We refer to these galaxies in the following as *back2* and *back1*, respectively.

Thus, together with the quasar, the *main* ($z = 0.704$) galaxy has potentially three background sightlines (quasar, *back1*, and *back2*) that can probe the CGM kinematics. In addition to the quasar, *back1* is a useful background source, as it has a very bright UV continuum.[2] *back2* is not a useful background source, due to intractable contamination from the close-by quasar. The orientation of all three sightlines w.r.t. the $z = 0.704$ galaxy is shown in Fig. 1(A) and listed in Table 1. The listed errors are resulting from the uncertainties on position angle and centroid of the *main* galaxy (cf. §3.2 and Appendix A).

3.2 The main galaxy's properties

The spectrum of the main $z = 0.704$ galaxy is shown in Fig. 2. The galaxy shows visibly weaker line emission than is typical for star-forming galaxies on the star forming "main sequence" (MS) at this redshift (e.g. Speagle et al. 2014; Boogaard et al. 2018). Quantitatively, we found the galaxy to have a stellar mass of $\log(M_*/\mathrm{M}_\odot) = 9.8^{+0.4}_{-0.0}$ and a star formation rate (SFR) of $0.5^{+0.3}_{-0.2}\,\mathrm{M}_\odot\,\mathrm{yr}^{-1}$.

The corresponding specific SFR (sSFR $= 0.07 \pm 0.06\,\mathrm{Gyr}^{-1}$) is $-0.6^{+0.2}_{-0.6}$ dex (or $\approx 1.5\sigma$) below the MS prediction for $z = 0.70$ (Boogaard et al. 2018). This means our galaxy is similar to 'green valley' galaxies.

We determined the stellar mass and SFR as in paper II. In short, we estimated M_* from SED fitting using our custom code CONIECTO (see also Zabl et al. 2016) on 13 pseudo-medium band filters created from the MUSE spectrum.[3] Other values obtained from the SED fit are listed in Table 2. The (instantaneous) SFR was determined starting from the measured [O II] flux, correcting it for extinction using the Calzetti et al. (2000) law with the strength of the extinction estimated from the $M_* - E(B-V)$ relation of Garn & Best (2010), and converted to a SFR using the Kewley et al. (2004) relation.

We estimated the [O II] flux from a fit to the [O II] morpho-kinematics using the 3D fitting tool GALPAK3D (Bouché et al. 2015). This fit provided us also with a best-fit estimate of the kinematics (see Table 2). The steps involved in the GALPAK3D fitting were again identical to those described in paper II. However, as the [O II] flux is low for this galaxy, it was not possible to robustly measure the kinematics and morphology (inclination in particular) based on [O II] alone.[4] Thus, we decided to constrain the inclination, i, using a continuum map in a pseudo r-band image created from the MUSE cube. We determined the galaxy morphology, including i and position angle, PA, from this continuum map using GALFIT (Peng et al. 2010). Further, we used the appropriate Moffat PSF for the r-band as determined from the quasar. The fit was complicated by systematic residuals from the close-by quasar. Nevertheless, we could obtain a robust estimate of $i = 71 \pm 5\,\mathrm{deg}$ and $PA = 37 \pm 8\,\mathrm{deg}$. Details about the fit and the method to estimate the uncertainties are given in Appendix A. Finally, we fit the [O II] kinematics with GALPAK3D using i and the PA as obtained from the continuum ($i = 71\,\mathrm{deg}$, $PA = 37\,\mathrm{deg}$).

3.3 Absorption in CGM of the main galaxy

The CGM around the $z = 0.704$ main galaxy can be probed in absorption at multiple locations using the spectra of the background quasar and the *back1* galaxy. While high spectral resolution spectroscopy is only available for the quasar, we can use the MUSE data cube to probe Mg II absorption with the same spectral resolution in both sightlines.

3.3.1 Mg II *absorption at the resolution of MUSE*

Mg II is the strongest among the CGM metal absorption lines covered by the MUSE data at this redshift and hence the most useful to probe the CGM with low signal-to-noise (S/N) background galaxy sightlines. We show in panel E of Fig. 1 the observed z=0.704 Mg II absorption both for the quasar (orange) and the *back1* (red) sightlines (Mg II λ2796 -dotted-, Mg II λ2803 -solid-). The figure shows that Mg II absorption is not only visible in the quasar sightline ($\mathrm{EW}_0^{\lambda 2796} = 2.7$ Å), as per selection, but also in the *back1* sightline ($\mathrm{EW}_0^{\lambda 2796} = 2.0$ Å).

Despite the moderate spectral resolution ($190\,\mathrm{km\ s}^{-1}$ at 4700 Å), the absorption profiles encode interesting information. First, a velocity shift is clearly visible between the two sightlines. The absorption in the *back1* galaxy sightline is redshifted w.r.t. that in the quasar sightline by $84 \pm 17\,\mathrm{km\ s}^{-1}$, with the absorption in the two sightlines centred at $110 \pm 17\,\mathrm{km\ s}^{-1}$ and $25.8 \pm 0.4\,\mathrm{km\ s}^{-1}$, respectively. We obtained these velocity measurements by simultaneously fitting both components of the Mg II doublet with Gaussians. Second, we measured a $\mathrm{EW}_0^{\lambda 2796}/\mathrm{EW}_0^{\lambda 2803}$ ratio close to one in both sightlines. This means the Mg II absorption is strongly saturated.[5] Third, we find that the flux reaches almost zero at peak absorption. For both sightlines, this means, when accounting for the resolution of MUSE, that the Mg II absorption is spread over a large velocity range. For the extended galaxy sightline (*back1*), this further means that the Mg II coverage must be complete over the extent of the aperture from which we have extracted the background spectrum. The non-circular extraction aperture, which was chosen to optimize the S/N, included 29 spatial pixels corresponding to an area of $1.2\,\mathrm{arcsec}^2$.

[2] The full spectral energy distribution (SED) of the z=1.42 *back1* galaxy is shown in the Supplementary Appendix of paper II. The galaxy has a $M_{2800\,\text{Å}}$ absolute total magnitude of -20.8, which is slightly brighter than the characteristic Schechter magnitude at its redshift (Dahlen et al. 2007).

[3] Different from paper II, we assumed a delayed τ star formation history (SFH) (SFR $\propto t \times exp(-t/\tau)$, with t being the elapsed cosmic time since the galaxy started forming stars.

[4] This is the reason why the galaxy was not part of the sample in paper III.

[5] The $\mathrm{EW}_0^{\lambda 2796}/\mathrm{EW}_0^{\lambda 2803}$ ratio for optically thin absorption is 2:1.

Table 1. Geometrical orientation of the system. (1) Background object ID; (2) redshift; (3) impact parameter measured from *main* $z = 0.70$ foreground galaxy [kpc at redshift of *main*]; (4) azimuthal angle w.r.t. the major axis of *main* [deg]; (5) magnitude in 1″ diameter aperture measured in pseudo-V filter created from MUSE data.

Object (1)	z (2)	b (3)	α (4)	m_V (5)
Quasar	1.484	16.8 ± 0.7	81 ± 8	18.5
Back1	1.417	8.8 ± 0.7	-109 ± 9	24.7
Back2	0.809	20.5 ± 0.7	115 ± 8	24.0

3.3.2 *Absorption at the resolution of UVES*

In the previous section, we compared Mg II absorption along both the galaxy and the quasar sightline at the same moderate spectral resolution of MUSE. For the quasar sightline, we can use the high spectral resolution UVES spectrum (8 km s^{-1}) to study the kinematics in more detail. In Fig. 3, we show one line each for Mn II, Zn II, Fe II, Mg II, Mg I, Na I. This is a subset of the low ionization lines covered by the UVES spectrum. In addition to the data, a multi-component fit is shown. For this fit, the positions and total number of velocity components in the absorption system were derived from all identified species. Their wavelength positions were then fixed to avoid degeneracy with blended features. For individual elements, only a subset of components was selected and fitted with a single Gaussian each with the evolutionary algorithm described in Quast et al. (2005) and applied in Wendt & Molaro (2012).

As expected from the MUSE spectrum, the Mg II λ2796 absorption covers a broad velocity range - from -130 to 205 km s^{-1} - and is strongly saturated for most of this range. Unsaturated or weakly saturated lines, such as the Mg I λ2852 line, are more useful to identify sub-structures. Based on these transitions, we identified three main components, which are indicated in Fig. 3 and labeled with *A* (red), *B* (magenta), and *C* (orange). They are offset from the systemic redshift of the foreground galaxy by -49, 10, and 100 km s^{-1}, respectively.

From the UVES spectrum, [Zn II/Fe II] is measured for components A+B to be $\sim 1.1 \pm 0.1$,[6] which indicates a significant amount of depletion for intervening systems (De Cia et al. 2016) of ≈ 0.3 dex (≈ 1.5 dex) for Zn (Fe), respectively. This level of depletion is also associated with more metal rich absorption systems with [Zn/H] around 1/2 solar (De Cia et al. 2016).

4 CGM TOY MODEL

Mg II absorption around a galaxy is, in observations, predominantly found either along the galaxy's minor or major axis (e.g. Bordoloi et al. 2011; Bouché et al. 2012; Kacprzak et al. 2012; Nielsen et al. 2015; Martin et al. 2019), see also paper II and paper III. A natural explanation for this dichotomy is a simple model of a bi-conical outflow perpendicular to the galaxy disk and an extended gaseous disk aligned with the galaxy disk. This picture has gained support both from the theoretical and observational sides, i.e. predictions from cosmological hydro simulations (winds e.g., Dubois & Teyssier 2008; Shen et al. 2012, 2013, disks: e.g., Pichon et al. 2011; Kimm et al. 2011; Shen et al. 2013; Danovich et al. 2015; Stewart et al. 2011, 2017) and directly observed emission properties of local galaxies (winds: e.g., Veilleux et al. 2005 for a review, disks: e.g., Putman et al. 2009; Wang et al. 2016; Ianjamasimanana et al. 2018).

In the following, we investigate a toy model implementation for kinematics and morphology of a disk+outflow model to interpret the observed absorption features in both the quasar and *back1* sightlines.

[6] The assumed solar abundances are adopted from Jenkins 2009 (based on Lodders 2003).

Table 2. Physical properties of the foreground galaxy (*main*). For further details see §3.2 and paper II. (1) [O II] flux obtained from GALPAK3D fit; (2) nebular extinction from $E(B-V)$-M_* relation; (3) nebular extinction from SED fit; (4) instantaneous SFR from 1 & 2; (5) instantaneous SFR from SED fit; (6) stellar mass from SED fit; (7) rest-frame B absolute magnitude from best fit SED model; (8) distance from the MS (assuming MS from Boogaard et al. 2018); (9) age of galaxy from SED fit (time since onset of star-formation); (10) decay time in delayed τ SFH from SED fit; (11) rotation velocity from GALPAK3D fit; (12) velocity dispersion from GALPAK3D fit; (13) virial velocity from $v_{vir} = v_{max}/(1.1 \pm 0.3)$; (14) virial radius from v_{vir}; (15) virial mass from v_{vir}; (16) virial mass from abundance matching (Behroozi et al. 2010); (17) escape velocities at position of quasar/*back1* sightline assuming a truncated isothermal sphere.

Row	Property	Value	Unit
(1)	$f_{[O II]}$	$(1.5 \pm 0.1) \times 10^{-17}$	erg s^{-1} cm^{-2}
(2)	E(B-V) (M_*)	$0.24^{+0.12}_{-0.09}$	mag
(3)	E(B-V) (SED)	$0.00^{+0.42}_{-0.00}$	mag
(4)	SFR ($f_{[O II]}$)	$0.5^{+0.3}_{-0.2}$	$M_\odot$ yr^{-1}
(5)	SFR (SED)	$0.3^{+9.6}_{-0.0}$	$M_\odot$ yr^{-1}
(6)	M_* (SED)	$9.8^{+0.4}_{-0.0}$	log($M_\odot$)
(7)	B	-19.6	mag
(8)	$\delta(MS)$	$-0.6^{+0.2}_{-0.6}$	dex
(9)	*age*	$9.5^{+0.0}_{-0.3}$	log(yr)
(10)	τ	$8.7^{+0.6}_{-0.1}$	log(yr)
(11)	v_{max}	118 ± 21	km s^{-1}
(12)	σ_0	38 ± 15	km s^{-1}
(13)	v_{vir}	107^{+44}_{-30}	km s^{-1}
(14)	r_{vir}	120^{+50}_{-34}	kpc
(15)	M_{vir} (from M_*)	$11.6^{+0.2}_{-0.1}$	log($M_\odot$)
(16)	M_{vir} (from kin.)	$11.5^{+0.5}_{-0.4}$	log($M_\odot$)
(17)	v_{esc} (qso/*back1*)	261 / 287	km s^{-1}

4.1 Model parameters

4.1.1 *Biconical outflow*

For the outflow model, we assume that a galaxy launches winds from its central region into a bi-conical outflow with half-opening angle θ_{out}. We allow the cone to be devoid of Mg II within an inner opening angle, θ_{in}, as indicated by larger samples of wind pairs (e.g. papers I & III, Bouché et al. (2012)). For the wind kinematics, we assume that the gas flows outward radially with an outflow velocity,

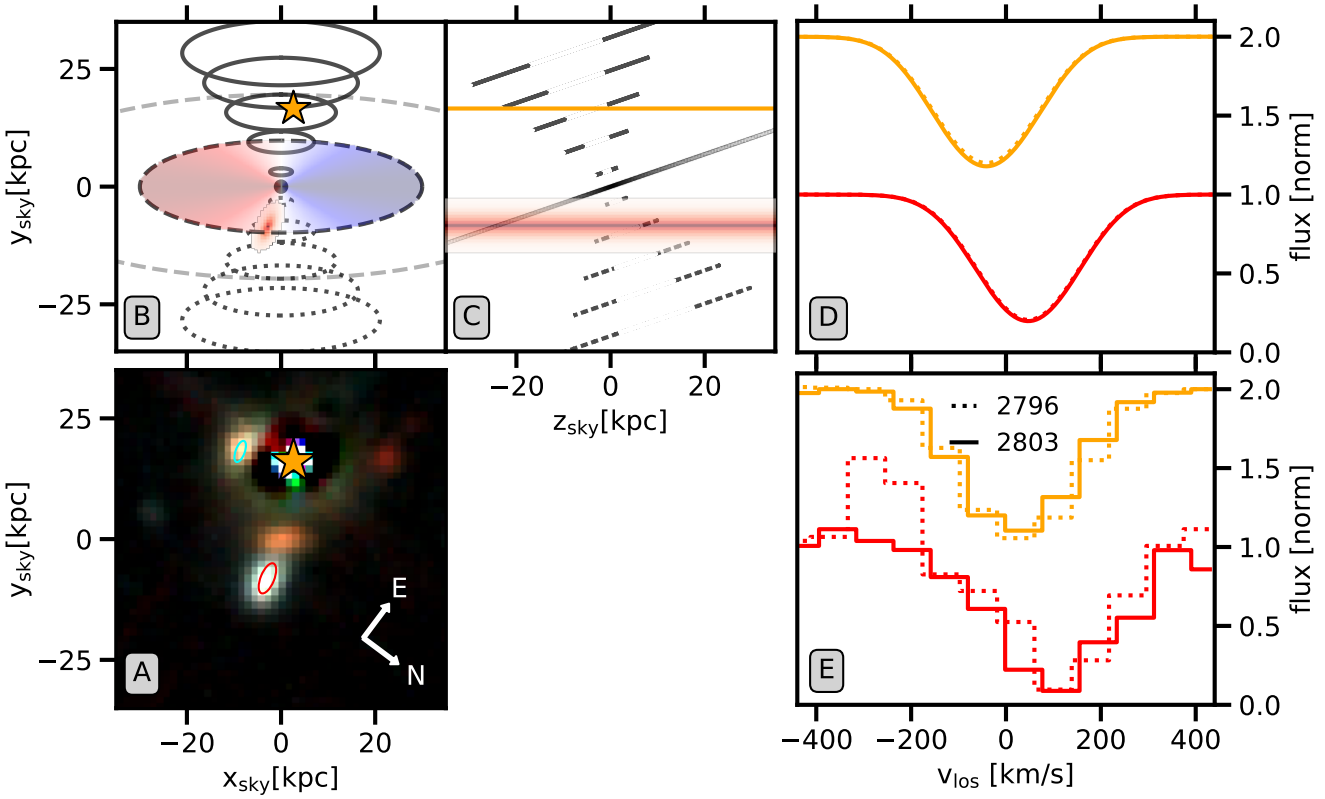

Figure 1. Comparison between data and model for the Mg II absorption seen in the MUSE spectrum for two sightlines through the CGM of the *main* galaxy. **A:** 9″.8 × 9″.8 field, corresponding to 70 kpc × 70 kpc at $z = 0.70$, around the *main* foreground galaxy shown as color image with pseudo z',r',V broad-band MUSE images in the red, green, and blue channel, respectively. The quasar was subtracted, but residuals are visible. The *main* foreground galaxy (center) is surrounded by three bright background sources: the *quasar* towards the top (orange star), the bright galaxy towards the bottom (*back1*; red ellipse), and the second galaxy close to the quasar (*back2*; cyan ellipse). **B:** View of the assumed CGM model (see §4) on the sky plane. The approaching outflow cone is indicated as solid concentric circles, while the receding outflow cone is indicated by dotted circles. For the extended gas disk, the rotation line-of-sight velocity field is overlaid. The orientation is identical to panel A and the positions of the quasar and *back1* are indicated by the orange dot and the red surface-brightness ellipse, respectively. **C:** Geometry of the same model as in B, but here with the line-of-sight direction on the x-axis. The point-source sightline for the quasar (orange) and the extended sightline for *back1* (red) are indicated. The cone is hollow in the inner part. **D:** Mg II λλ2796, 2803 line-of-sight kinematics simulated at the resolution of MUSE based on the model shown in panels B&C and described in §5.3 for the quasar (orange; offset by +1) and *back1* (red) sightlines, respectively. Both the 2796 Å and 2803 Å lines of the Mg II doublet are shown (dotted/solid; almost identical). The model parameters are listed as 'disk + wind' model in Table 4. **E:** Mg II line-of-sight kinematics measured with MUSE in the background quasar (orange; offset by +1) and galaxy spectra (red), respectively. The zero-velocity corresponds to the systemic redshift of the *main* galaxy ($z = 0.70344$) as measured from the [O II] emission.

v_{out}, that does not change with distance from the galaxy. From mass conservation, this constant velocity necessitates a radial density $\rho(r) \propto r^{-2}$, which is normalized at 1 kpc with $\rho_1 \equiv \rho(1\text{kpc})$. We also account for random motions of the encountered gas with σ_{gas}. Moreover, we assume that the gas does not change its ionization state and that it is smoothly distributed. Thus the wind parameters are θ_{out}, θ_{in}, v_{out} and ρ_1 and σ_{gas} which are listed Table 3.

The cone opening angle θ_{out} is ≈ 30 deg, and the inner cone is $\theta_{in} \approx 15$ deg, consistent with typical values in paper III. The outflow velocity v_{out} is assumed to be 150 km s^{-1}, corresponding to the typical v_{out} in paper III. The intrinsic dispersion σ_{gas} is chosen somewhat arbitrarily to be 10 km s^{-1}. All parameters of the fiducial model are summarized in Table 4.

4.1.2 Extended gas disk

However, as the sightlines are at relatively small impact parameters (at 8.8 kpc and 16.8 kpc), a contribution from a thick extended gas disk cannot be ruled out. We model this extended gaseous disk as an exponential profile with scale length h_r in radial direction. In the direction perpendicular to the disk (z-direction), we assume an exponential profile with scale height h_z. The gas density is normalized at the disk mid-plane in the disk center with ρ_0. For the disk's kinematics, we assume that the gas is rotating parallel to the disk midplane with a circular velocity v_{circ}, which we assume to be identical to v_{max} from the galaxy rotation. In addition, the gas velocity vector can also have a radial infall component, v_r, which is added to the tangential component

Table 3. Summary of model parameters in the CGM toy model (cf. §4).

	Property	Description	Unit
		Sightline	
(1)	i	Inclination	[deg]
		Biconocial outflow	
(2)	$\theta_{\rm out}$	Outer (half-)cone opening angle	[deg]
(3)	$\theta_{\rm in}$	Inner (half-)cone opening angle	[deg]
(4)	$v_{\rm out}$	Outflow velocity	[km s^{-1}]
(5)	$\sigma_{\rm gas}$	Gas velocity dispersion	[km s^{-1}]
(6)	ρ_1	Density at norm radius (Mg II)	[cm^{-3}]
		Extended gas disk	
(7)	$v_{\rm circ}$	Circular velocity of gas	[km s^{-1}]
(8)	$v_{\rm r}$	Radial velocity of gas	[km s^{-1}]
(9)	$h_{\rm r}$	Exponential scale length (radial)	[kpc]
(10)	$h_{\rm z}$	Exponential scale length (vertical)	[kpc]
(11)	$\sigma_{\rm gas}$	Gas velocity dispersion	[km s^{-1}]
(12)	ρ_0	Density at $r = 0$ and $z = 0$ (Mg II)	[cm^{-3}]

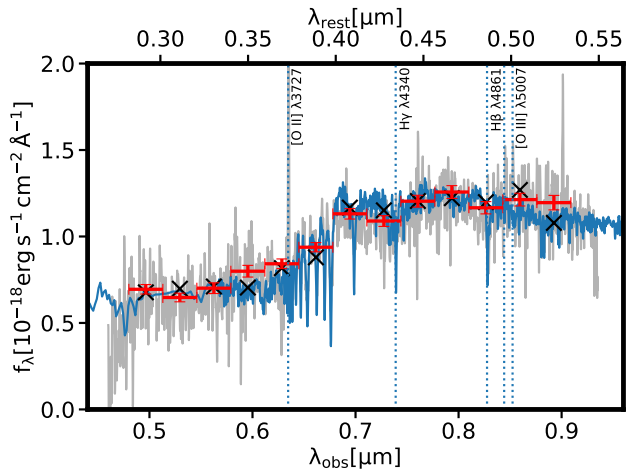

Figure 2. Best-fit SED model (blue) for the main foreground galaxy compared to the observed spectrum (grey, smoothed with $FWHM = 8.8$ Å Gaussian). The fit was done using pseudo-photometry for 13 medium-band filters created from the spectrum itself. The red errorbars indicate the filter-averaged flux densities in these filters, with the horizontal bars indicating the width of the filters. The black crosses show the flux-densities in the same filters as obtained from the best-fit SED. While the SED fitting was done including emission lines and the shown model medium band flux-densities include this contribution, the best-fit SED is shown without the emission to avoid visual confusion with the actual emission lines.

keeping $v_{\rm circ}$ constant. [7] The disk parameters are $v_{\rm circ}$, $v_{\rm r}$, $\sigma_{\rm gas}$, $h_{\rm z}$ and ρ_0 which are summarized in Table 3.

The circular velocity $v_{\rm circ}$ is given by the kinematics of the host galaxy as described in § 3.2. The stellar scale height h_z of distant galaxies is typically 1 *kpc*, as suggested by studies of edge-on disks in *Hubble* deep fields (e.g. Elmegreen & Elmegreen 2006; Elmegreen et al. 2017). We assume that the extended cool gas disk probed by Mg II has similar scale height ($h_z = 1$ kpc). The gas dispersion, $\sigma_{\rm gas}$, is assumed to be ~ 10 km s^{-1} appropriate for the temperature of low-ionization gas (e.g. Churchill et al. 2003). The density ρ_0 will be adjusted in order to match the absorption optical depth for Mg I.

4.2 Simulated absorption lines

We use our code CGMPY to calculate the Mg II absorption profile which the outflow cones and/or the extended gas disk would imprint on a background source. In short, the code calculates for each of small steps (= 1 pc) along the line-of-sight (LOS) the LOS velocity, $v_{\rm los;step}$, and the column density, $N_{\rm step}$, which can subsequently be converted to an optical depth, $\tau_{\rm step}(v_{\rm los})$. The full $\tau(v_{\rm los})$ distribution for the complete sightline is then obtained by summing up the $\tau_{\rm step}(v_{\rm los})$ from each step and each component without the turbulent velocity dispersion $\sigma_{\rm gas}$. We account for this random motions of the gas ($\sigma_{\rm gas}$) by convolving the optical depth distribution with a Gaussian of the selected $\sigma_{\rm gas}$. Finally, the absorption profile is obtained by taking $e^{-\tau(v_{\rm los})}$ and convolving with the instrumental line spread function (LSF).

In the case of an extended sightline (such as for '*back1*'), the absorption from the extended object is calculated by taking the average over individual sightlines flux weighted over an elliptical aperture centered on the galaxy (for *back1* with an area of ~ 1 arcsec^2).

5 DISCUSSION

Here, we describe how the toy model discussed in §4 performs in discribing our data. However, we stress that we do

[7] The circular and the radial moving gas are here asssumed to add to a single components as in paper II, but unlike in Bouché et al. (2016), where the same gas has both a radial and infalling component.

Table 4. The choice for each of the parameters in Table 3 as used for the five models described in §5 and shown in Fig. 4.

Model	i (1)	$\theta_{\rm out}$ (2)	$\theta_{\rm in}$ (3)	$v_{\rm out}$ (4)	$\sigma_{\rm gas}$ (5)	ρ_1 (6)	$v_{\rm circ}$ (7)	$v_{\rm r}$ (8)	$h_{\rm r}$ (9)	$h_{\rm z}$ (10)	$\sigma_{\rm gas}$ (11)	ρ_0 (12)
Fiducial wind	71	35	15	150	10	8×10^{-5}	–	–	–	–	–	–
Slow wind	71	35	15	75	10	8×10^{-5}	–	–	–	–	–	–
Disk	71	–	–	–	–	–	118	–	5	1	10	3×10^{-3}
Disk w. infall	71	–	–	–	–	–	118	-40	5	1	10	3×10^{-3}
Disk + wind	71	35	15	100	10	8×10^{-5}	118	–	5	1	10	3×10^{-3}

not expect this simple toy model to account for all data features nor do we attempt to formally fit it to the data. Thus, if the model can, at least approximately, explain most of the absorption in *both* background sightlines, the simple toy model can be viewed as a description of the *main* galaxy's CGM.

5.1 The fiducial (wind-only) model

We first tested the performance of a fiducial biconical outflow-only model (cf. §4.1.1) given that both the quasar and *back1* are positionned along the minor axis of the host galaxy, i.e. without an extended gas disk.

Here, the model's orientation is set by the measurement of the galaxy's inclination i (see §3.2). However, as the sign of the galaxy inclination cannot be constrained with the available data (see e.g. Ho & Martin 2019), we were left with two possible solutions. Here, we choose the sign of the inclination such that the absorbing gas in the cones is outflowing. This outflow assumption requires that redshifted absorption must originate from the far-side cone, and consequently, the *back1* galaxy sightline crosses this far-side cone. Panels B and C of Fig. 1 show the adopted orientation.

For our 'fiducial' outflow model, we assume a value for $\theta_{\rm out}$ (35 deg), which is at the higher end of typical values found in paper III. We made this choice, to ensure very high coverage over the extended *back1* galaxy sightline in the model, as required by the observed absorption strength (see §3.3.1).

In Fig. 4 (row 1 - 'Fiducial wind'), we overlay the resulting absorption profiles over the UVES and MUSE data for the 'qso' (Cols 1, 2 and 3) and '*back1*' (Col. 4) sightlines. Column 1 (2) show the model for the quasar sightlines for Mg II (Mg I), respectively, where we scaled the Mg I density by 1/600 compared to Mg II according to Lan & Fukugita (2017). Comparing our UVES data to the model for the quasar sightlines shown in Cols. 1 ans 2, we find that the absorption is made of two separate components which arise from the assumption of an empty inner cone. These two components might correspond to components *A* and *B* in the observed spectrum (see §3.3.2). Comparing our MUSE data and the fiducial wind model (Cols 3 and 4), we find that the model and data match qualitatively for the blue- (red-) shifted absorptions in the quasar (galaxy) sightlines absorption shown in Col. 3 (4), respectively. However, there are some discrepancies between the model and the data.

The main discrepancy is that the wind model cannot explain the redshifted third component C. Another discrepancy is that, for the quasar absorption, the model predicts a blue-shift (-75 km s^{-1}) whereas the observed absorption is close to systemic at $\approx +25$ km s^{-1}.

A model with lower outflow velocity ($v_{\rm out} \approx 75$ km s^{-1}) would better match to components A and B in the Mg I absorption (Fig. 4; row 2 - 'Slow wind'). However, it underpredicts the redshift compared to the Mg II data in the *back1* galaxy sightline. Note that this potential velocity difference between the two sightlines could indicate deceleration of the gas with distance from the galaxy, as the quasar sightline is probing gas at a larger impact parameter than the *back1* sightline does (16.8 kpc vs 8.8 kpc). Strong, non-gravitational, deceleration in an outflow could be due to drag forces (in observations e.g., Martini et al. 2018; in simulations e.g., Oppenheimer et al. 2010). However, this interpretation would require the strong assumption that the two opposite cones have the same velocity profile.

5.2 Disk model

Given the limitations of the fiducial wind only-model, and the relatively small impact parameters, we discuss the extended gaseous disk model presented in §4.1.2. Indeed, the two minor-axis sightlines cross the disk midplane at galactocentric radii of 26 kpc ($0.21\,r_{\rm vir}$) and 51 kpc ($0.42\,r_{\rm vir}$), within the extent of co-rotating gas disks from paper II and Ho et al. (2017). Before discussing a potential combination of wind and disk-model, we test whether a simple thick disk model similar to Steidel et al. (2002); Kacprzak et al. (2010); Ho et al. (2017) can potentially explain all absorption on its own.

In Fig. 4 (row 3 - 'Disk'), we overlay the resulting absorption profiles over the MUSE and UVES data as before. Comparing the UVES data to our model shows that a thick disk model can only explain component B in the Mg I spectrum.[8] As for the wind model, the thick disk model cannot explain the redshifted third component C. However, component A in the UVES spectrum could be accounted for with an extension of this disk model with a radial inflow component (shown in row 4 of Fig. 4 - 'Disk + infall'). The observed velocity of -49 km s^{-1} would require a radial velocity component of $v_{\rm r} \approx -40$ km s^{-1} $= -0.4\,v_{\rm vir}$.[9] Such a radial

[8] We note that a very thin disk would have a narrower profile, hence a lower equivalent width, and also a lower velocity shift than a thick disk. This is, because a sightline crossing a thick disks encounters different velocities at different heights above the disk, up to $\sin(i)v_{\rm circ}$ (e.g. Steidel et al. 2002).

[9] $v_{\rm r} \approx -40$ km s^{-1} is enough to match the observed blueshift of component A, because the model has also a contribution from the rotational component ($v_{\rm circ}$).

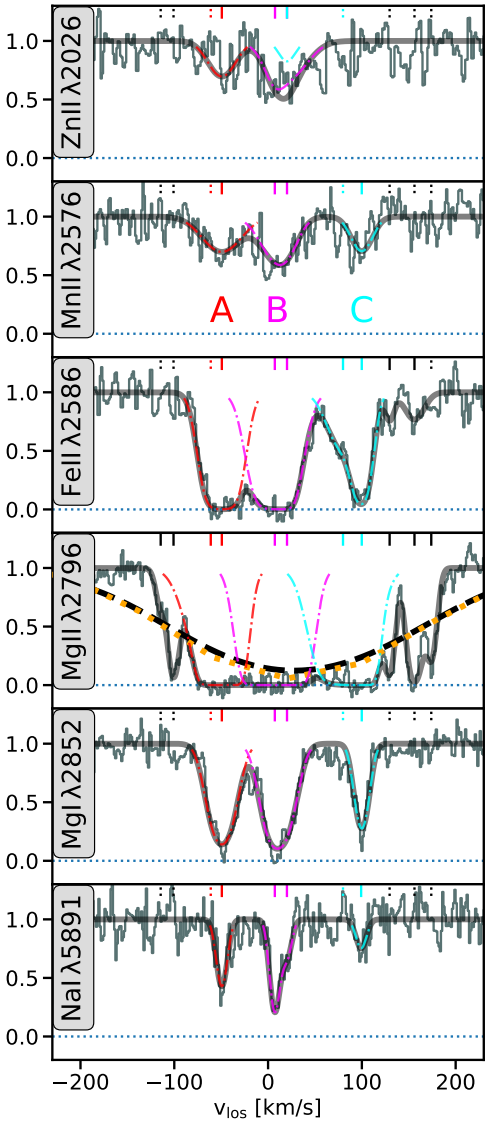

Figure 3. Absorption in the quasar sightline at the redshift of *main* measured with the high spectral resolution VLT/UVES data. **Panels 1-6 from the top:** The observed absorption is shown for multiple species, with a multi-component model fit (thick grey line) overplotted over the data. The velocity components considered in the fit are indicated as little bars near the top of the panels, where a dotted bar indicates that the component was not used for the specific line. Three main kinematic components, A, B, C, can be clearly identified from the unsaturated lines. The contribution of the three components, as measured from the multi-component fit, is shown by different colors. For comparison, the panel for Mg II λ2796 also shows the MUSE spectrum (orange dotted; identical to panel E in Fig. 1) and the UVES spectrum artificially degraded to the resolution of MUSE (black dashed).

inflow velocity is feasible, based on results from simulations (e.g. Rosdahl & Blaizot 2012; van de Voort & Schaye 2012; Goerdt & Ceverino 2015; Ho et al. 2019) and observational studies targeting the major axis sightlines (e.g. Bouché et al. 2013, 2016; Rahmani et al. 2018a, paper II).

5.3 Combined disk and wind

The observed absorption might be a combination of aborption from both a disk and an outflow component. As discussed in §5.1, the ouflow component alone, a faster wind (150 km s^{-1}) matches better the observed absorption in the *back1* sightline, while a slower wind (75 km s^{-1}) matches better the absorption in the qso sightline. For the following, we assume a wind speed of 100 km s^{-1} as a compromise to match approximately both sightlines with a single wind speed. Fig. 4 (row 5 - 'Disk + wind') shows the resulting absorption profile when combining the disk and this wind toy model (The same model is also shown in Fig. 1, panel D). While imperfect, the toy model is qualitatively in agreement with the observed spectra, apart from component C. Component C might be an unrelated component, similar to the high-velocity clouds (HVC) seen around the Milky Way (e.g., Wakker & van Woerden 1997 for a review). In summary, a plausible interpretation of the observed kinematics in the two sightlines is absorption in a bi-conical outflow with a potential disk contribution.

5.4 Feasibility of the outflow

As discussed in §3.2, the SFR of the *main* galaxy is low compared to star-forming galaxies with similar mass at similar redshift. This raises the question whether the energy and the momentum that are required to explain the wind are at all feasible. To answer this question, we estimated the mass outflow rate, $\dot{M}_{\rm out}$, the energy-outflow rate, $\dot{E}_{\rm out}$, and the momentum outflow rate, $\dot{p}_{\rm out}$. These estimates can subsequently be compared to the estimated SFR and the corresponding energy and momentum deposition rates from supernovae (SNe).

We estimated $\dot{M}_{\rm out}$ for the bi-conical outflow of cool gas using Eq. 5 from paper III. As inputs to the equation we assumed $\theta_{\rm out} = 35\,{\rm deg}$, $\theta_{\rm in} = 15\,{\rm deg}$, $b = 15\,{\rm kpc}$, $v_{\rm out} = 100\,{\rm km\ s^{-1}}$, $\log(N_{\rm HI}/{\rm cm^{-2}}) = 20.0$. Here, we estimated the H I column density using the $EW_0^{\lambda2796}$ - H I relation from Ménard & Chelouche (2009) and Lan & Fukugita (2017), which has an uncertainty of around 0.3 dex. Using these values in the equations we obtain $\dot{M}_{\rm out} = 2.0\,{\rm M_\odot\ yr^{-1}}$. This corresponds with the assumed $v_{\rm out} = 100\,{\rm km\ s^{-1}}$ to $\dot{E}_{\rm out} = 6.0 \times 10^{39}\,{\rm erg\,s^{-1}}$ and $\dot{p}_{\rm out} = 1.3 \times 10^{33}\,{\rm g\,cm\,s^{-1}}$.

A comparison of $\dot{M}_{\rm out}$ to the estimated SFR allows us to infer the mass-loading ($\eta = \dot{M}_{\rm out}/{\rm SFR}$), which characterizes the efficiency of a star formation powered wind to remove gas from the galaxy. Assuming that the wind was powered by the current SFR of $0.5\,{\rm M_\odot\ yr^{-1}}$, we infer $\eta \approx 4$. This value can be compared to measurements of η both from individual estimates (quasar sightlines e.g. paper III, Bouché et al. 2012; Schroetter et al. 2015; down the barrel: e.g. Weiner et al. 2009; Martin et al. 2012; Rubin et al. 2014; Sugahara et al. 2017), indirect observational evidence (e.g. Zahid et al. 2014; Mitra et al. 2015), or simulations (e.g. Hopkins et al. 2012; Muratov et al. 2015). For the mass and redshift of our main galaxy, the values in these studies typically range from $\eta \approx$ 1–10 (see also discussion in paper III). Hence, we conclude that the η corresponding to our preferred model seems feasible.

A direct comparison of the measured $\dot{E}_{\rm out}$ and $\dot{p}_{\rm out}$ to the momentum and energy injected by SNe leads to a simi-

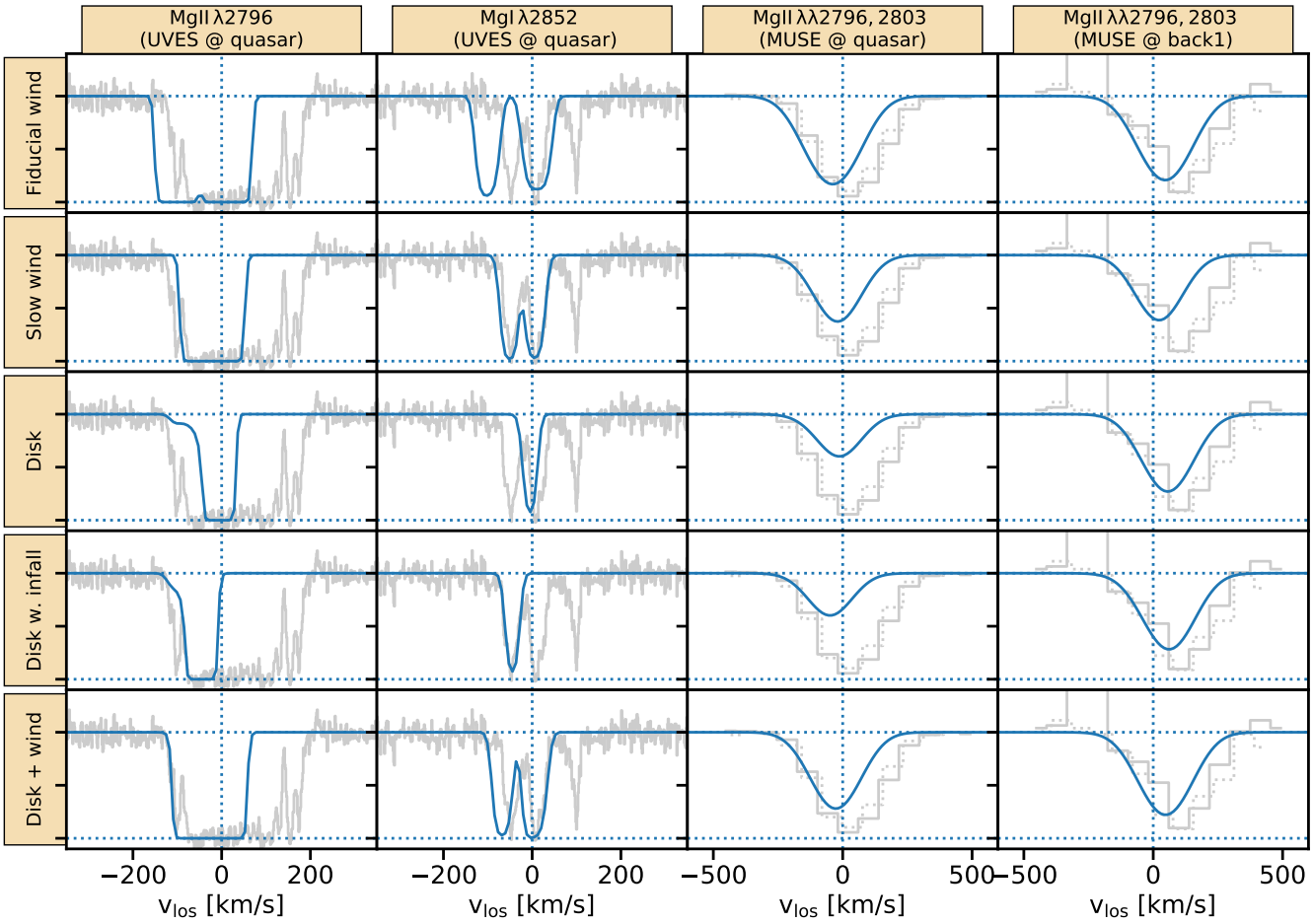

Figure 4. Comparison between data and various models. Eeach row shows a different model, as listed in Table 4. In each panel the light grey curve is the observed absorption, while the blue line shows the modeled absorption. The first two columns show Mg II λ2796 (column 1) and Mg I λ2852 (column 2) in the quasar sightline at the resolution of UVES. The third and fourth column show Mg II λ2796, 2803 for the quasar sightline (column 3) and the *back1* galaxy sightline (column 4) at the resolution of MUSE. Here, the solid line is Mg II λ2796 (data and model) and the dotted line is Mg II λ2803 (data).

lar conclusion. Per $1 M_\odot\,yr^{-1}$ of star formation SNe deposit mechanical energy and momentum with rates of approximately $1.6 \times 3 \times 10^{41}\,erg\,s^{-1}$ (from Chisholm et al. 2017 based on Leitherer et al. 1999) and $1.6 \times 2 \times 10^{33}\,g\,cm\,s^{-1}$ (Murray et al. 2005).[10] This means that our measured values correspond to energy and momentum loading of 3% and 80%, respectively. These values are comparable to those found by Chisholm et al. (2017) for a sample of local star-forming galaxies when considering the relevant mass range.[11]

Finally, we note that the actual loading factors could be smaller. The SFR might have been higher at the time when the wind was launched. It would have taken the wind $\approx$ 200 Myr ($\approx$ 100 Myr) to travel to the quasar (*back1*) sightline, assuming $v_{out} = 100\,km\,s^{-1}$. With the limited available data we cannot rule out that there was a significant burst of star-formation about 200–300 Myr ago, as motivated by tests with non-parmetric SFHs with PPXF (Cappellari & Emsellem 2004; Cappellari 2017).

6 CONCLUSIONS

It is now statistically well established that there is a dichotomy in the spatial distribution of the cool circumgalactic medium (CGM) gas probed through Mg II absorption, where the two components have been identified as arising in an extended gas disk and a bi-conical outflow. In this paper, we present a rare chance alignment of a quasar and a UV-bright background galaxy at relatively small impact parameters (16.8 and 8.8 kpc) from a $z = 0.7$ foreground galaxy. As the two sightlines are close to the foreground galaxy's projected minor axis, but on opposite sides of the major axis, the configuration is ideal to test the bi-conical outflow component. Through studying the observed absorption both in MUSE and UVES data from the MEGAFLOW survey, and comparison to modeled absorption, we reached the following conclusions:

[10] Factor 1.6 is to convert from the Salpeter (1955) to the Chabrier (2003) IMF.
[11] We have only included the cool phase of the outflow, so the total loading factors could be higher.

- Both sightlines show very strong Mg II absorption ($EW_0^{\lambda 2796} > 2.0$ Å).
- We find a significant velocity shift of $84 \pm 17\,\mathrm{km\ s^{-1}}$ between the two sightlines.
- The observed velocity shift is in broad agreement with a bi-conical outflow toy model with a moderate outflow velocity of $\approx 100\,\mathrm{km\ s^{-1}}$, possibly combined with a disk model.
- The foreground galaxy has a relatively low sSFR ($0.07 \pm 0.06\,\mathrm{Gyr^{-1}}$), which puts the galaxy 0.6 dex below the MS at $z = 0.7$. However, the mass-loading (η) required to explain the modelled outflow is not unrealistic high ($\eta \approx 4$). Moreover, the sSFR may have been higher when the wind was launched, $\sim 10^8$ yr.

This study presented a 'tomographic' study (i.e. with multi-sightline) of the CGM around an individual galaxy in the distant Universe ($z \approx 0.7$), and hence goes beyond the statistical inference from single sightline samples. While we find the data to be in broad agreement with our fiducial CGM model, we cannot rule out alternative explanations. A comparison of the CGM model to larger samples of rare multi-sightline cases, including cases with even more sightlines as e.g. provided by background groups or gravitationally lensed arcs (e.g. Lopez et al. 2018, 2019), will be an important test for our assumed geometry. Additionally, it will be necessary to test the geometry against observations of the CGM in emission (e.g. Finley et al. 2017; Rupke et al. 2019).

ACKNOWLEDGEMENTS

This paper is dedicated to the memory of our wonderful friend and colleague, Hayley Finley.

We thank the anonymous referee for a constructive report, which helped to improve the quality of this manuscript. This study is based on observations collected at the European Southern Observatory under ESO programmes 097.A-0138(A), 097.A-0144(A), 0100.A-0089(A). This work has been carried out thanks to the support of the ANR FOGHAR (ANR-13-BS05-0010), the ANR 3DGasFlows (ANR-17-CE31-0017), the OCEVU Labex (ANR-11-LABX-0060), and the A*MIDEX project (ANR-11-IDEX-0001-02) funded by the "Investissements d'avenir" French government program.

This work made use of the following open source software: GalPak3D (Bouché et al. 2015), ZAP (Soto et al. 2016), MPDAF (Piqueras et al. 2017), matplotlib (Hunter 2007), NumPy (van der Walt et al. 2011; Oliphant 2007), Astropy (Astropy Collaboration et al. 2013).

REFERENCES

Astropy Collaboration et al., 2013, A&A, 558, A33
Bacon R., et al., 2006, Msngr, 124, 5
Bacon R., et al., 2010, in Society of Photo-Optical Instrumentation Engineers (SPIE) Conference Series. p. 8, doi:10.1117/12.856027
Bacon R., et al., 2017, A&A, 608, A1
Behroozi P. S., Conroy C., Wechsler R. H., 2010, ApJ, 717, 379
Bergeron J., 1988, in IAU Symp. 130: Large Scale Structures of the Universe. pp 343–+
Bergeron J., Boissé P., 1991, A&A, 243, 344
Bergeron J., Stasińska G., 1986, A&A, 169, 1
Boogaard L. A., et al., 2018, A&A, 619, A27
Bordoloi R., et al., 2011, ApJ, 743, 10
Bouché N., Murphy M. T., Péroux C., Csabai I., Wild V., 2006, MNRAS, 371, 495
Bouché N., Hohensee W., Vargas R., Kacprzak G. G., Martin C. L., Cooke J., Churchill C. W., 2012, MNRAS, 426, 801
Bouché N., Murphy M. T., Kacprzak G. G., Péroux C., Contini T., Martin C. L., Dessauges-Zavadsky M., 2013, Science, 341, 50
Bouché N., Carfantan H., Schroetter I., Michel-Dansac L., Contini T., 2015, AJ, 150, 92
Bouché N., et al., 2016, ApJ, 820, 121
Bowen D. V., Chelouche D., Jenkins E. B., Tripp T. M., Pettini M., York D. G., Frye B. L., 2016, ApJ, 826, 50
Calzetti D., Armus L., Bohlin R. C., Kinney A. L., Koornneef J., Storchi-Bergmann T., 2000, ApJ, 533, 682
Cappellari M., 2017, MNRAS, 466, 798
Cappellari M., Emsellem E., 2004, PASP, 116, 138
Chabrier G., 2003, PASP, 115, 763
Chen H.-W., Kennicutt Jr. R. C., Rauch M., 2005, ApJ, 620, 703
Chen H.-W., Helsby J. E., Gauthier J.-R., Shectman S. A., Thompson I. B., Tinker J. L., 2010, ApJ, 714, 1521
Chisholm J., Tremonti C. A., Leitherer C., Chen Y., 2017, MNRAS, 469, 4831
Churchill C. W., Vogt S. S., Charlton J. C., 2003, AJ, 125, 98
Crighton N. H. M., Morris S. L., Bechtold J., Crain R. A., Jannuzi B. T., Shone A., Theuns T., 2010, MNRAS, 402, 1273
D'Odorico V., Cristiani S., D'Odorico S., Fontana A., Giallongo E., Shaver P., 1998, A&A, 339, 678
Dahlen T., Mobasher B., Dickinson M., Ferguson H. C., Giavalisco M., Kretchmer C., Ravindranath S., 2007, ApJ, 654, 172
Danovich M., Dekel A., Hahn O., Ceverino D., Primack J., 2015, MNRAS, 449, 2087
De Cia A., Ledoux C., Mattsson L., Petitjean P., Srianand R., Gavignaud I., Jenkins E. B., 2016, A&A, 596, A97
Dekker H., D'Odorico S., Kaufer A., Delabre B., Kotzlowski H., 2000, in Iye M., Moorwood A. F., eds, Proc. SPIEVol. 4008, Optical and IR Telescope Instrumentation and Detectors. pp 534–545, doi:10.1117/12.395512
Dubois Y., Teyssier R., 2008, A&A, 477, 79
Ellison S. L., Ibata R., Pettini M., Lewis G. F., Aracil B., Petitjean P., Srianand R., 2004, A&A, 414, 79
Elmegreen B. G., Elmegreen D. M., 2006, ApJ, 650, 644
Elmegreen B. G., Elmegreen D. M., Tompkins B., Jenks L. G., 2017, ApJ, 847, 14
Finley H., et al., 2017, A&A, 605, A118
Garn T., Best P. N., 2010, MNRAS, 409, 421
Goerdt T., Ceverino D., 2015, MNRAS, 450, 3359
Ho S. H., Martin C. L., 2019, arXiv e-prints, p. arXiv:1901.11182
Ho S. H., Martin C. L., Kacprzak G. G., Churchill C. W., 2017, ApJ, 835, 267
Ho S. H., Martin C. L., Turner M. L., 2019, ApJ, 875, 54
Hopkins P. F., Quataert E., Murray N., 2012, MNRAS, 421, 3522
Hunter J. D., 2007, Computing in Science and Engineering, 9, 90
Ianjamasimanana R., Walter F., de Blok W. J. G., Heald G. H., Brinks E., 2018, AJ, 155, 233
Jenkins E. B., 2009, ApJ, 700, 1299
Kacprzak G. G., Churchill C. W., Ceverino D., Steidel C. C., Klypin A., Murphy M. T., 2010, ApJ, 711, 533
Kacprzak G. G., Churchill C. W., Evans J. L., Murphy M. T., Steidel C. C., 2011a, MNRAS, 416, 3118
Kacprzak G. G., Churchill C. W., Barton E. J., Cooke J., 2011b, ApJ, 733, 105
Kacprzak G. G., Churchill C. W., Nielsen N. M., 2012, ApJ, 760, L7
Kacprzak G. G., et al., 2014, ApJ, 792, L12
Kewley L. J., Geller M. J., Jansen R. A., 2004, AJ, 127, 2002

Kimm T., Devriendt J., Slyz A., Pichon C., Kassin S. A., Dubois Y., 2011, preprint, (arXiv:1106.0538)
Lan T.-W., Fukugita M., 2017, ApJ, 850, 156
Lan T.-W., Mo H., 2018, ApJ, 866, 36
Lan T.-W., Ménard B., Zhu G., 2014, ApJ, 795, 31
Lanzetta K. M., Bowen D., 1990, ApJ, 357, 321
Lanzetta K. M., Turnshek D. A., Wolfe A. M., 1987, ApJ, 322, 739
Leitherer C., et al., 1999, ApJS, 123, 3
Lodders K., 2003, ApJ, 591, 1220
Lopez S., Reimers D., Rauch M., Sargent W. L. W., Smette A., 1999, ApJ, 513, 598
Lopez S., Ellison S., D'Odorico S., Kim T. S., 2007, A&A, 469, 61
Lopez S., et al., 2018, Nature, 554, 493
Lopez S., et al., 2019, arXiv e-prints, p. arXiv:1911.04809
Martin C. L., Shapley A. E., Coil A. L., Kornei K. A., Bundy K., Weiner B. J., Noeske K. G., Schiminovich D., 2012, ApJ, 760, 127
Martin C. L., Ho S. H., Kacprzak G. G., Churchill C. W., 2019, ApJ, 878, 84
Martini P., Leroy A. K., Mangum J. G., Bolatto A., Keating K. M., Sandstrom K., Walter F., 2018, ApJ, 856, 61
Ménard B., Chelouche D., 2009, MNRAS, 393, 808
Mitra S., Davé R., Finlator K., 2015, MNRAS, 452, 1184
Muratov A. L., Kereš D., Faucher-Giguère C.-A., Hopkins P. F., Quataert E., Murray N., 2015, MNRAS, 454, 2691
Murray N., Quataert E., Thompson T. A., 2005, ApJ, 618, 569
Muzahid S., 2014, ApJ, 784, 5
Muzahid S., Kacprzak G. G., Churchill C. W., Charlton J. C., Nielsen N. M., Mathes N. L., Trujillo-Gomez S., 2015, ApJ, 811, 132
Nestor D. B., Turnshek D. A., Rao S. M., 2005, ApJ, 628, 637
Nielsen N. M., Churchill C. W., Kacprzak G. G., Murphy M. T., 2013a, ApJ, 776, 114
Nielsen N. M., Churchill C. W., Kacprzak G. G., 2013b, ApJ, 776, 115
Nielsen N. M., Churchill C. W., Kacprzak G. G., Murphy M. T., Evans J. L., 2015, ApJ, 812, 83
Oliphant T. E., 2007, Computing in Science and Engineering, 9, 10
Oppenheimer B. D., Davé R., Kereš D., Fardal M., Katz N., Kollmeier J. A., Weinberg D. H., 2010, MNRAS, 406, 2325
Peng C. Y., Ho L. C., Impey C. D., Rix H.-W., 2010, AJ, 139, 2097
Péroux C., Rahmani H., Arrigoni Battaia F., Augustin R., 2018, MNRAS, 479, L50
Pichon C., Pogosyan D., Kimm T., Slyz A., Devriendt J., Dubois Y., 2011, MNRAS, 418, 2493
Piqueras L., Conseil S., Shepherd M., Bacon R., Leclercq F., Richard J., 2017, preprint, (arXiv:1710.03554)
Putman M. E., et al., 2009, ApJ, 703, 1486
Quast R., Baade R., Reimers D., 2005, A&A, 431, 1167
Rahmani H., et al., 2018a, MNRAS, 474, 254
Rahmani H., et al., 2018b, MNRAS, 480, 5046
Rauch M., Sargent W. L. W., Barlow T. A., 1999, ApJ, 515, 500
Rosdahl J., Blaizot J., 2012, MNRAS, 423, 344
Rubin K. H. R., Prochaska J. X., Koo D. C., Phillips A. C., Martin C. L., Winstrom L. O., 2014, ApJ, 794, 156
Rubin K. H. R., et al., 2018, ApJ, 859, 146
Rupke D. S. N., et al., 2019, Nature, 574, 643
Salpeter E. E., 1955, ApJ, 121, 161
Schroetter I., Bouché N., Péroux C., Murphy M. T., Contini T., Finley H., 2015, ApJ, 804, 83
Schroetter I., et al., 2016, ApJ, 833, 39
Schroetter I., et al., 2019, MNRAS, 490, 4368
Shen S., Madau P., Aguirre A., Guedes J., Mayer L., Wadsley J., 2012, ApJ, 760, 50
Shen S., Madau P., Guedes J., Mayer L., Prochaska J. X., Wadsley J., 2013, ApJ, 765, 89
Soto K. T., Lilly S. J., Bacon R., Richard J., Conseil S., 2016, ZAP: Zurich Atmosphere Purge, Astrophysics Source Code Library (ascl:1602.003)
Speagle J. S., Steinhardt C. L., Capak P. L., Silverman J. D., 2014, ApJS, 214, 15
Steidel C. C., 1995, in Meylan G., ed., QSO Absorption Lines. ESO Astrophysics Symposia. Springer-Verlag, Berlin, Germany, p. 139
Steidel C. C., Sargent W. L. W., 1992, ApJS, 80, 1
Steidel C. C., Kollmeier J. A., Shapley A. E., Churchill C. W., Dickinson M., Pettini M., 2002, ApJ, 570, 526
Stewart K. R., Kaufmann T., Bullock J. S., Barton E. J., Maller A. H., Diemand J., Wadsley J., 2011, ApJ, 738, 39
Stewart K. R., et al., 2017, ApJ, 843, 47
Sugahara Y., Ouchi M., Lin L., Martin C. L., Ono Y., Harikane Y., Shibuya T., Yan R., 2017, ApJ, 850, 51
Tumlinson J., Peeples M. S., Werk J. K., 2017, Annual Review of Astronomy and Astrophysics, 55, 389
Veilleux S., Cecil G., Bland-Hawthorn J., 2005, ARA&A, 43, 769
Wakker B. P., van Woerden H., 1997, ARA&A, 35, 217
Wang J., Koribalski B. S., Serra P., van der Hulst T., Roychowdhury S., Kamphuis P., Chengalur J. N., 2016, MNRAS, 460, 2143
Weilbacher P. M., Streicher O., Urrutia T., Jarno A., Pécontal-Rousset A., Bacon R., Böhm P., 2012, in Society of Photo-Optical Instrumentation Engineers (SPIE) Conference Series. p. 0, doi:10.1117/12.925114
Weilbacher P. M., Streicher O., Urrutia T., Pécontal-Rousset A., Jarno A., Bacon R., 2014, in Manset N., Forshay P., eds, Astronomical Society of the Pacific Conference Series Vol. 485, Astronomical Data Analysis Software and Systems XXIII. p. 451 (arXiv:1507.00034)
Weilbacher P. M., Streicher O., Palsa R., 2016, MUSE-DRP: MUSE Data Reduction Pipeline, Astrophysics Source Code Library (ascl:1610.004)
Weiner B. J., et al., 2009, ApJ, 692, 187
Wendt M., Molaro P., 2012, A&A, 541, A69
Zabl J., Freudling W., Møller P., Milvang-Jensen B., Nilsson K. K., Fynbo J. P. U., Le Fèvre O., Tasca L. A. M., 2016, A&A, 590, A66
Zabl J., et al., 2019, MNRAS, 485, 1961
Zahid H. J., Torrey P., Vogelsberger M., Hernquist L., Kewley L., Davé R., 2014, Ap&SS, 349, 873
Zhu G., Ménard B., 2013, ApJ, 770, 130
van de Voort F., Schaye J., 2012, MNRAS, 423, 2991
van der Walt S., Colbert S. C., Varoquaux G., 2011, Computing in Science and Engineering, 13, 22

APPENDIX A: UNCERTAINTY ON INCLINATION AND POSITION ANGLE

In our analysis, we tied the orientation of our toy model (§4) to the orientation of the *main* foreground galaxy. Therefore, a robust measurement of position angle (PA) and inclination (i) is important. As discussed in §3.2, the measurement of the galaxy's morphology is somewhat complicated by residuals from the PSF subtraction. The residuals made a formal assessment of the uncertainties based on the χ^2 doubtful. Therefore, we preferred to rely on a visual assessment of the uncertainties. For this purpose we created GALFIT models deviating from the best fit model either in PA or inclination. Fig. A1 shows models and residuals all for the best-fit model, the $PA_{\rm best} - 15\,{\rm deg}$, $PA_{\rm best} + 15\,{\rm deg}$, $i_{\rm best} - 10\,{\rm deg}$, $i_{\rm best} + 10\,{\rm deg}$. Except for the modified PA or i, we used in each case identical morphological parameters to those in the

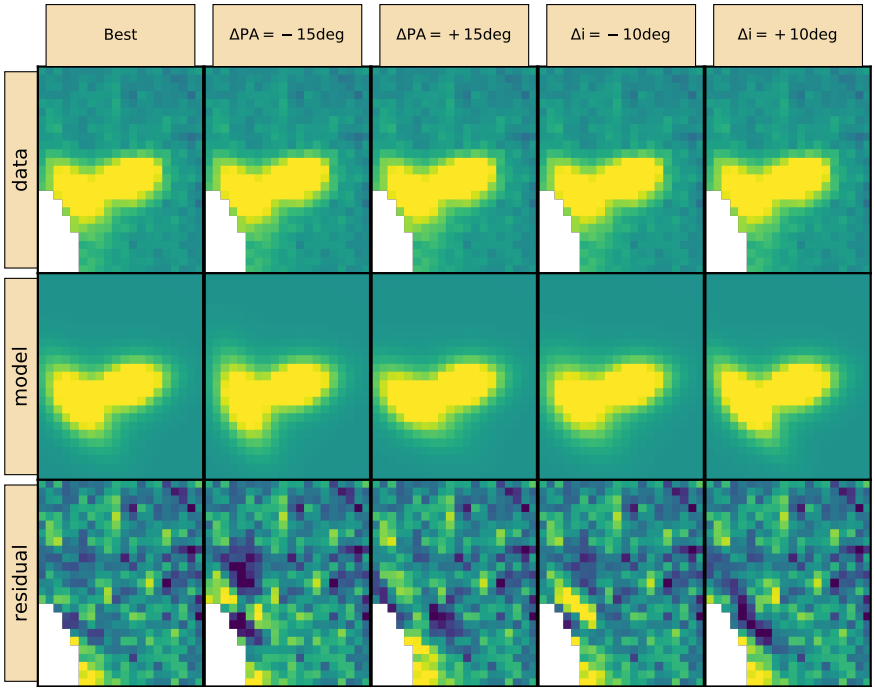

Figure A1. Data, GALFIT model, and residuals (data-model) are shown for each of five models in the top, center, and bottom row, respectively. The data, which are identical in each of the four columns, are a pseudo broadband r image created from the MUSE cube. The *main* foreground galaxy is to the left and the *back1* background galaxy is to the right (north is to the top, east to the left; different orientation from Fig. 1). The white region to the lower left masks residuals from the quasar subtraction. **Left column:** Best fit GALFIT model, where both *main* and *back1* were fit simultaneously. The *main* galaxy has best fit $PA_{\rm best} = 37\,$deg and $i_{\rm best} = 71\,$deg assuming a $n = 1$ Sersic profile. **Center left column:** This column and the other three columns show the best fit model with either the PA or i of the *main* galaxy adjusted. Here, $PA = PA_{\rm best} - 15\,$deg; **Center column:** $PA = PA_{\rm best} + 15\,$deg; **Center right column:** $i = i_{\rm best} - 10\,$deg; **Right column:** $i = i_{\rm best} + 10\,$deg.

best fit model. The only free fit parameter in each of the alternative models was the total flux. Both for $PA \pm 15\,$deg and $i \pm 10\,$deg the residuals are much stronger than for the best-fit model and the models seems essentially inconsistent with the data. Therefore, it seems plausible to define these PA and *incl* differences as 2σ uncertainties. In summary, we conclude therefore that the 1σ uncertainties for PA and i are 8 deg and 5 deg, respectively.

In addition to the uncertainty in PA and i, there is also a small uncertainty on the centroid. We estimated this uncertainty through comparison between the continuum centroid obtained from this GALFIT fit and the [O II] centroid obtained from GALPAK3D fit. We find a deviation of $0''.16$ between the two centroids. Therefore, we can assume as 1σ uncertainty $0''.1$ both in right ascension and declination.

APPENDIX B: IMPACT OF UNCERTAINTIES ON INCLINATION AND POSITION ANGLE ON MODELS

In this section, we asses the impact of the uncertainties for i and PA on the simulated absorption in our toy models.

In Fig. B1 we show the 'Slow wind' model (see. Table 4) with either i or PA changed compared to the fiducial values (row 1). Rows 2 and 3 show the result for changing the i by $\pm 5\,$deg (i.e., 66 deg and 76 deg), while keeping the fiducial value for the PA. Rows 4 and 5 show the impact of varying the PA of *main* by $\pm 10\,$deg. Assuming $\Delta PA \pm 10\,$deg means that the azimuthal angle α is changed by $\mp 10\,$deg both for the quasar and the *back1* sightline (equally) compared to the values stated in Table 1. All other parameters are kept identical to those listed for the 'Slow wind' model in Table 4 and shown in the first row of Fig. B1.

In general, the differences between the absorption profiles for these variants appear small. The strongest visible impact is for $\Delta PA = +10\,$deg (corresponding to $\alpha = 71\,$deg for quasar and $\alpha = -119\,$deg for *back1*). In this case, the Mg I absorption profile is not double-peaked and the Mg II absorption in the *back1* sightline is visibly weaker than in the fiducial model. The double peak is absent, because the distance from the minor axis is larger than in the fiducial case and, consequently, the quasar sightline does not cross the hollow part of the cone. The weaker Mg II absorption for *back1* is also a consequence of a larger distance from the minor axis. At $\alpha = -119\,$deg part of the extended *back1* galaxy sightline is no longer covered by the cone at all, which reduces the effective $\mathrm{EW}_0^{\lambda 2796}$.

In Fig B2, we test the impact of the same i and PA variations, but now for the 'Disk' model (see Table 4). Here, the differences in absorption strength appear stronger than in the wind case. This is especially the case for changes in i. Here, the strength varies - especially for the Mg I absorption in the quasar sightline - as the sightline crosses the disk

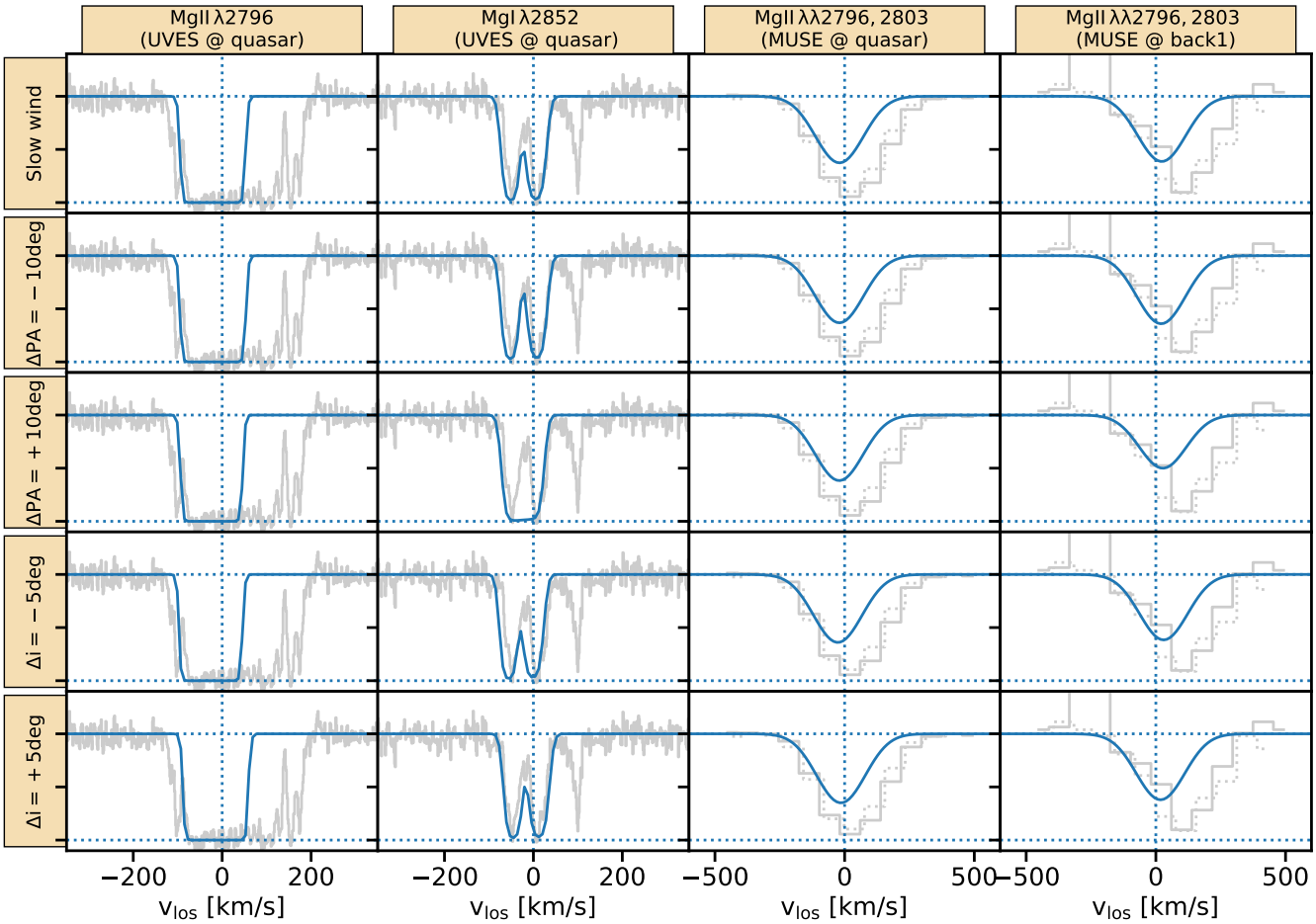

Figure B1. Comparison between modeled and observed absorption for the 'Slow wind' model assuming different inclinations and position angles. The first row is identical to row 2 in Fig. 4, where the best fit i and PA were assumed. Details about the content displayed in the four columns are given in the caption of Fig. 4. The subsequent rows (1-4) show the same model, but with i or PA changed by the values stated in the row labels. For further details, see Appendix B.

mid-plane at larger galacto-centric radii, the larger the i is. We note, though, that most of the changes could be compensated for by merely choosing a disk with higher density. For the variations with PA, the centroid of the absorption shifts, but only slightly.

In summary, we can conclude that the uncertainties on i and PA/α, as estimated in Appendix A, only subtly change our simulated profiles. Therefore, we can decide that our conclusions in §5 are not impacted by these uncertainties.

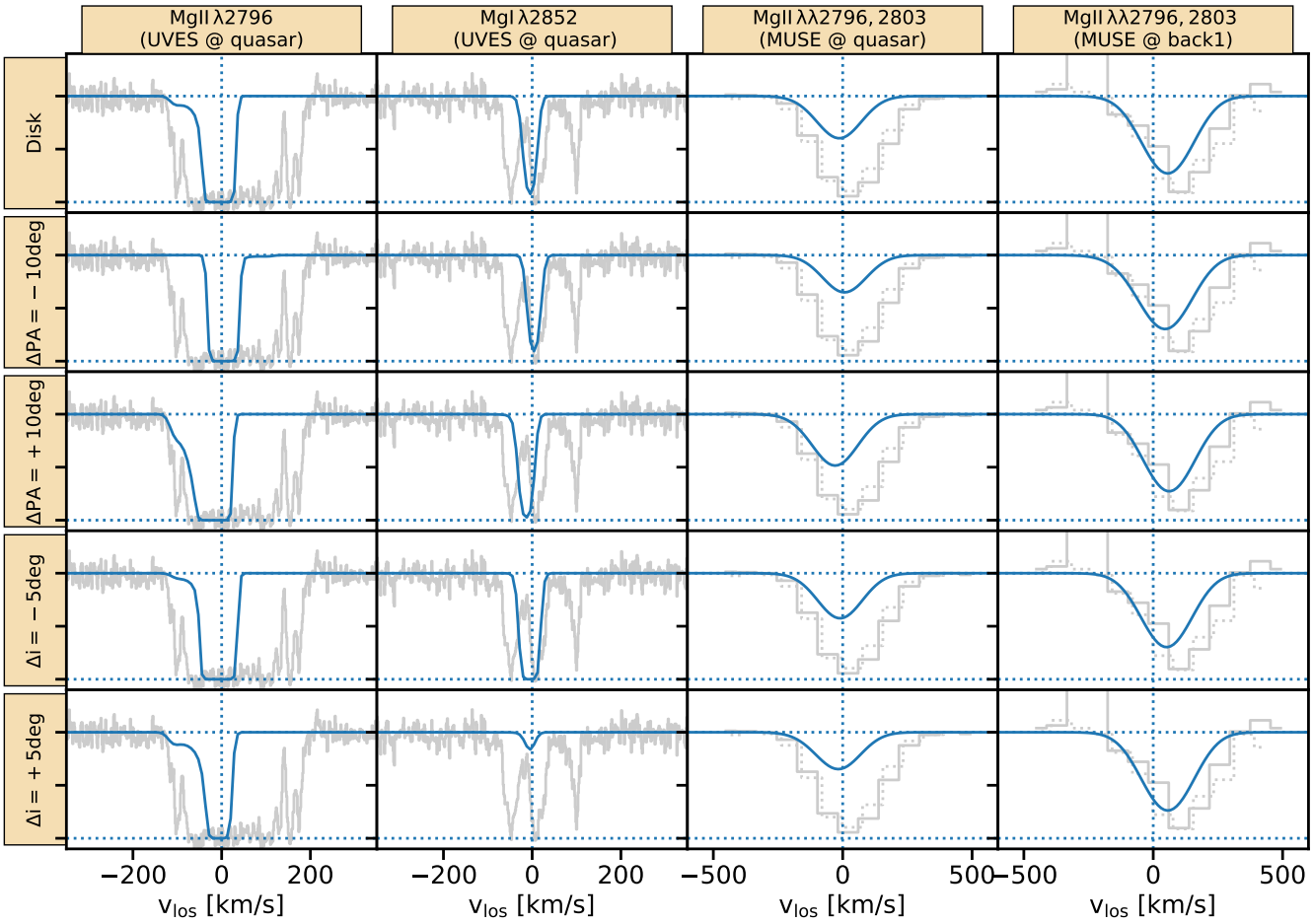

Figure B2. As Fig. B1, but here for the 'Disk' model (cf. row 3 in Fig. 4). For further details, see Appendix B.